Applied Physics Letters

Dual function spin-wave logic gates based on electric field control magnetic anisotropy boundary

Cite as: Appl. Phys. Lett. **120**, 142405 (2022); https://doi.org/10.1063/5.0089890
Submitted: 01 March 2022 • Accepted: 28 March 2022 • Published Online: 06 April 2022

Kang Wang, Shaojie Hu, Fupeng Gao, et al.

View Online

Export Citation

CrossMark

ARTICLES YOU MAY BE INTERESTED IN

Influence of diffusive transport on ultrafast magnetization dynamics
Applied Physics Letters **120**, 142402 (2022); https://doi.org/10.1063/5.0080383

Enhancement of damping-like field and field-free switching in Co/Pt bilayer films through quantitative engineering of anisotropy gradient
Applied Physics Letters **120**, 142401 (2022); https://doi.org/10.1063/5.0088548

Anomalous Hall effect superimposed in polycrystalline $SrRuO_3$ thick film
Applied Physics Letters **120**, 142404 (2022); https://doi.org/10.1063/5.0085391

QBLOX

1 qubit

Shorten Setup Time
Auto-Calibration
More Qubits

Fully-integrated
Quantum Control Stacks
Ultrastable DC to 18.5 GHz
Synchronized <<1 ns
Ultralow noise

100s qubits

visit our website >

© 2022 Author(s).

Dual function spin-wave logic gates based on electric field control magnetic anisotropy boundary

Cite as: Appl. Phys. Lett. **120**, 142405 (2022); doi: 10.1063/5.0089890
Submitted: 1 March 2022 · Accepted: 28 March 2022 ·
Published Online: 6 April 2022

Kang Wang,[1] Shaojie Hu,[1,2,a)] Fupeng Gao,[1] Miaoxin Wang,[1] and Dawei Wang[3]

AFFILIATIONS

[1]Center for Spintronics and Quantum Systems, State Key Laboratory for Mechanical Behavior of Materials, School of Materials Science and Engineering, Xi'an Jiaotong University, Xi'an, Shaanxi 710049, China
[2]Department of Physics, Kyushu University, 744 Motooka, Fukuoka 819-0395, Japan
[3]School of Microelectronics & State Key Laboratory for Mechanical Behavior of Materials, Xi'an Jiaotong University, Xi'an 710049, China

[a)]Author to whom correspondence should be addressed: shaojiehu@mail.xjtu.edu.cn

ABSTRACT

Spin waves (SWs) have been considered a promising candidate for encoding information with lower power consumption. Here, we propose dual function SW logic gates, one unit cell with two synchronized logic operation functions, based on the electric field controlling of the SW propagation in the Fe film of a Fe/$BaTiO_3$ heterostructure by the motion of a magnetic anisotropy boundary. We show micromagnetic simulations to validate the AND–OR and NAND–NOR logic gates. Our research may find a path for simplifying integrated logic circuits using such dual function SW logic gates.

© 2022 Author(s). All article content, except where otherwise noted, is licensed under a Creative Commons Attribution (CC BY) license (http://creativecommons.org/licenses/by/4.0/). https://doi.org/10.1063/5.0089890

With the rapid development in the miniaturization of electronic devices, power consumption has become one important issue because of the unbearable Joule heating.[1,2] To overcome this issue, seeking new charge-neutral information carriers has spurred great attention. One representative charge-neutral information carrier is spin angular momentum, the electron's another degree of freedom. Spin waves (SWs), the collective spin angular momentum excitations in a magnetically ordered material and their associated quanta, magnons, are considered the promising information carrier for the next-generation lower power consumption, higher speed, and higher density devices. The phase,[3–6] amplitude,[7–10] and polarization[11,12] of SWs can be employed to encode information. Generally, the nanostructured SW logic gates are designed on the uniform magnetized ferromagnetic materials by using all kinds of methods to control the propagation of SWs, including the magnetic field,[10] electric current,[7–9] and voltage.[13,14]

The logic gates based on an electric field or voltage can be easily programmable and compatible with nanoscale microwave devices.[15] Rana and Otani[14] have proposed SW XNOR and universal NAND logic gates based on the voltage-controlled magnetic anisotropy (VCMA), which mainly arises from the change of an electronic occupation state near the interface between the magnetic films and nonmagnetic heavy metals controlled by the voltage.[15–17] Magnetoelectric effects[18–20] provide another path for electric-field control of SWs in multiferroic materials.[21,22] The most representative multiferroic system is artificial multiferroic materials. The single-crystalline ferroelectric barium titanate ($BaTiO_3$) membrane demonstrated super-elasticity and ultraflexibility properties.[23] This indicates that the lifetime of transformation of the ferroelectric domain may be over the generally expected for the thin membrane. Both the interfacial and bulk magnetoelectric coupling in Fe/$BaTiO_3$ have been studied by first-principles calculations and experiments.[24–26] Recently, electric field controlled spin wave propagation had been experimentally demonstrated in an artificial multiferroic Fe/$BaTiO_3$ heterostructure.[27] Magnetoelectric effects could help us to design many more functional SW logic gates based on a $BaTiO_3$ based multiferroic structure. Here, the dual function SW logic gates, one unit cell with two synchronized logic operation functions, are proposed by controlling the motion of the magnetic anisotropy boundary (MAB) in an epitaxial Fe film on the ferroelectric $BaTiO_3$ substrate with altering in-plane and out-of-plane polarization

© Author(s) 2022

domains. The AND–OR gate and NAND–NOR gate are validated by micromagnetic simulation.

We perform micromagnetic simulations by MuMax3[28] to study the propagation of Damon–Eshbach (DE) SWs[29] in the epitaxial Fe film on the ferroelectric $BaTiO_3$ substrate. Figure 1(a) shows one unit structure in our simulation, including one 2 nm thick Fe layer, 100 nm thick $BaTiO_3$, and the bottom electrode layer. The width and length of the structure are 800 and 2000 nm, respectively. The magnetic Fe layer includes uniaxial and cubic magnetic anisotropy regions via inverse magnetostriction owing to the different strains between the Fe film and two kinds of domains in the $BaTiO_3$ layer.[30] The easy axis of uniaxial magnetic anisotropy on top of the in-plane ferroelectric a-domain is along the y axis, while the easy axes of cubic anisotropy on top of the out-of-plane ferroelectric c-domain are along the direction with 45° to the x axis, as shown by the white double head arrows. The MAB is at the middle of the Fe film ($x = 0$, along the y axis) and is pinned on the ferroelectric domain wall of the $BaTiO_3$ substrate. The width of MAB in the Fe film is the same to the ferroelectric domain wall in $BaTiO_3$ [2–5 nm (Refs. 31–33)], which is far smaller than the wavelength of SWs (several hundred nanometers). So, we neglect the width of the MAB in simulation. The parameters of the Fe film used in simulation are the following:[34] saturation magnetization $M_s = 1.7 \times 10^6$ A/m, exchange stiffness constant $A_{ex} = 2.1 \times 10^{-11}$ J/m, and Gilbert damping constant $\alpha = 0.01$. The uniaxial and cubic magnetic anisotropy constants are the experiment values[27] of $K_u = 1.5 \times 10^4$ J/m^3 and $K_c = 4.4 \times 10^4$ J/m^3. The cell size is $2 \times 2 \times 2$ nm^3, which is smaller than the exchange length ($l_{ex} \approx 3.4$ nm). In order to avoid SWs' reflection at the boundary, the damping is set to 1 at both ends (width = 100 nm) of the Fe film. An external magnetic field $\mu_0 H_{ext} = 100$ mT is applied to avoid the formation of the magnetic domain wall and to magnetize the Fe film along the y axis. To obtain the dispersion relation of the DE SWs in uniaxial and cubic anisotropy regions, a sinc based exciting field, $\mathbf{h}(t) = h_0 \mathrm{sinc}(2\pi f_c(t - t_0))\hat{e}_z$, with $\mu_0 h_0 = 10$ mT, $f_c = 50$ GHz, and $t_0 = 5$ ns, is applied locally to a $2 \times 800 \times 2$ nm^3 central section of the Fe film, which is the SW source port (S) as indicated by the red region in Fig. 1(a). The dispersion relation[35,36] of SWs can be obtained by performing a two-dimensional Fourier transform on m_x ($m_x = M_x/M_s$), as shown in Fig. 1(b). The curve of the left branch is the dispersion relation of SWs propagating along the negative direction of the x axis in the uniaxial anisotropy region, and the right branch is the dispersion relation of SWs propagating along the positive direction of the x axis in the cubic anisotropy region. The theoretical curves of SW dispersion relations are calculated by adopting Eqs. (S4) and (S5) in the supplementary material. The difference in ferromagnetic resonance frequencies in the two anisotropy regions determines the working frequency range for the proposed device, $\frac{\gamma\mu_0}{2\pi}\sqrt{\left(\mathrm{H_{ext}} - \frac{2\mathrm{K_c}}{\mu_0 \mathrm{M_s}}\right)\left(\mathrm{H_{ext}} + \frac{\mathrm{K_c}}{\mu_0 \mathrm{M_s}} + \mathrm{M_s}\right)} < f < \frac{\gamma\mu_0}{2\pi}\sqrt{\left(\mathrm{H_{ext}} + \frac{2\mathrm{K_u}}{\mu_0 \mathrm{M_s}}\right)\left(\mathrm{H_{ext}} + \frac{2\mathrm{K_u}}{\mu_0 \mathrm{M_s}} + \mathrm{M_s}\right)}$, which is dominated by the anisotropy energy of the two regions. It is clear to show that the SWs are only excited in the cubic anisotropy region in the frequency range of 9.5 GHz $< f <$ 14.5 GHz. To further clarify the property, we excite SWs at the source port with a sinusoidal field $\mathbf{h}(t) = h_0 \sin(2\pi f t)\hat{e}_z$ with $\mu_0 h_0 = 10$ mT and a fixed $f = 12.6$ GHz. A snapshot of the M_x component of the magnetization taken at $t = 4$ ns is presented in Fig. 1(c). SWs only propagate in the region with cubic anisotropy.

An out-of-plane electric field controlling of ferroelectric domain wall motion can realize the movement of the MAB.[34] When the electric field is along the direction of the polarization in the c-domain, the c-domain will expand while the a-domain shrinks by the lateral domain wall motion. Suppose the electric field is inverse to the direction of the polarization in the c-domain. In that case, the c-domain will shrink, and the a-domain expands. So, the electric field can drive the ferroelectric domain wall's motion, thus driving the concurrent motion of the MAB. The velocity of the MAB, that is, the velocity of the ferroelectric domain wall driven by an electric field pulse, can be up to 1000 m/s.[37,38] Because the wall velocity is still smaller than the speed of sound in $BaTiO_3$ [$v_{sound} = 2000$ m/s (Ref. 39)], the strain state can be considered quasistatic during the motion of the ferroelectric domain wall, and the strength and symmetry of the magnetic anisotropy are invariant during the MAB back and forth. The velocity v of the MAB is implemented by shifting the MAB over one discretization cell ($\delta x = 2$ nm) during each time window $\delta t = \delta x/v$. In the simulation, the velocity of MAB is 1000 m/s under the electric field 31.4 MV/m obtained by applying 3.14 V perpendicular voltage, which is inferred from previous experimental results.[37]

Figure 2(a) shows the motion of the MAB driven by the voltage pulse, and Figs. 2(b)–2(d) show the schematics of the model and the snapshots of M_x when the MAB at $x = -600$, -100, and 400 nm, respectively. The SWs with $f = 12.6$ GHz are excited from the source

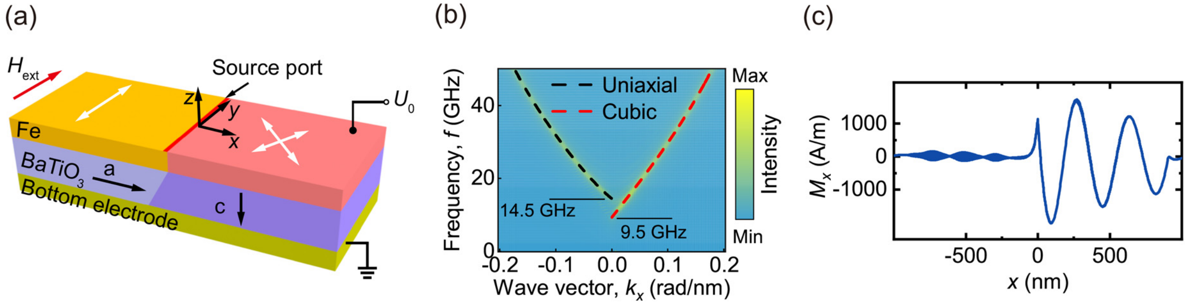

FIG. 1. (a) Schematic of the simulation model. The Fe film is grown on $BaTiO_3$ with the alternating in-plane polarization a-domain and out-of-plane polarization c-domain. The origin of the coordinate system is set at the center of the Fe film. (b) The image plot of the dispersion relation of the SWs. The dashed lines are theoretically calculated results. (c) A snapshot of the M_x component of the magnetization taken at $t = 4$ ns, $y = -1$ nm with a fixed $f = 12.6$ GHz.

© Author(s) 2022

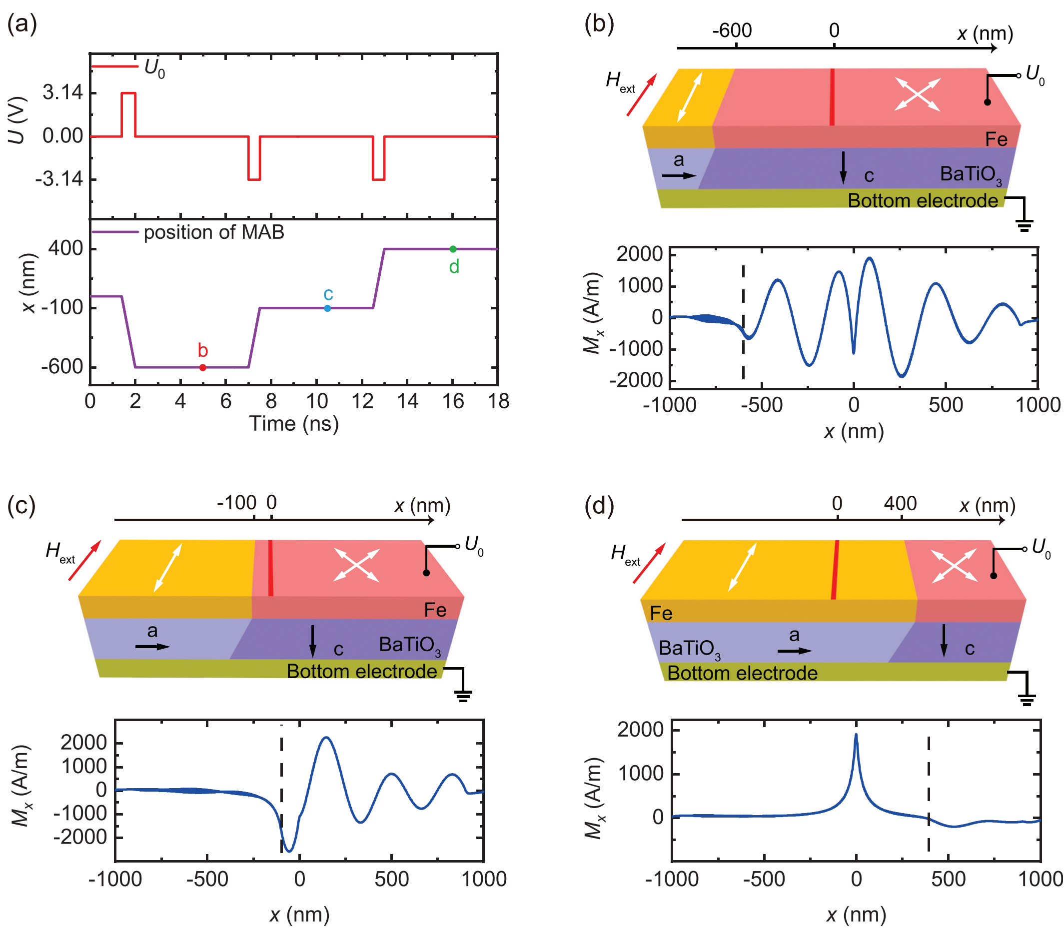

FIG. 2. (a) The position variation of the MAB with the voltage pulse. (b), (c), and (d) are the schematics of model and the snapshots of M_x taken at $y = -1$ nm when MAB at $x = -600$, -100, and 400 nm [adopting the coordinate system in Fig. 1(a)], respectively. The dashed lines mark the position of the MAB.

port. The position of the MAB is driven to $x = -600$ nm by using the positive electric voltage (1.4–2 ns) shown in Fig. 2(a). As expected, the SWs are blocked in an uniaxial anisotropy region shown by the snapshot of SWs taken at $t = 5$ ns in Fig. 2(b). After applying one negative pulse voltage (7–7.5 ns), the MAB moves to the position $x = -100$ nm. The SWs only propagate in the cubic anisotropy region from the snapshot of M_x taken at $t = 10.5$ ns, shown in Fig. 2(c). When another 0.5 ns negative voltage pulse is applied (12.5–13 ns), the MAB moves to the position $x = 400$ nm, and the SW source port is out of the cubic anisotropy region. There are no SWs in the Fe film. Thus, the transmission and block of SWs in the Fe film can be controlled by voltage through driving the motion of the MAB. Based on this unique property, we propose the design of dual function SW logic gates.

Figure 3(a) is the schematic of the dual function AND–OR gate, which includes two input ports (A and B), two output ports (C and D), and a source port of SWs. Initially, the MAB is set at $x = 400$ nm parallel to the y axis. The positions of input A and B ports are arbitrary on top of the Fe film. In order to make the two input ports independent, the B port includes a time delay unit, which can delay the voltage pulse for 0.5 ns. The output ports C and D take the x component of magnetization at regions (498 nm $< x <$ 500 nm, -2 nm $< y <$ 0 nm) and (-500 nm $< x < -498$ nm, -2 nm $< y <$ 0 nm), respectively, as indicated by the black square regions. Magnetic tunnel junctions can perform this function and convert SW signals to electrical signals. An external magnetic field $\mu_0 H_{ext} = 100$ mT is applied to magnetize the Fe film along the y axis, and a sinusoidal field $\mathbf{h}(t) = h_0 \sin(2\pi f t)\hat{e}_z$ with $\mu_0 h_0 = 10$ mT and $f = 12.6$ GHz is set at the source port. The bottom electrode is grounding.

The simulation results of the AND–OR gate with different inputs are shown in Figs. 3(b)–3(e). The simulation result of A = 0 and B = 0 is shown in Fig. 3(b). Obviously, the MAB remains still at position $x = 400$ nm, because there is no electric field across $BaTiO_3$. The outputs of C and D are both small amplitudes representing "0" due to the blocking of SWs shown in Fig. 2(d). The simulation result of A = 1 and B = 0 is shown in Fig. 3(c). The input "1" signal includes one 0.5 ns positive voltage pulse and 0.5 ns negative voltage pulse as shown in Fig. 3(c). The positive pulse is used to start logical operation by driving the MAB moving 500 nm along the negative direction of the x axis in 0.5 ns, while the negative pulse is used to reset the position of the MAB. The related motion of MAB and output signals of the two ports

© Author(s) 2022

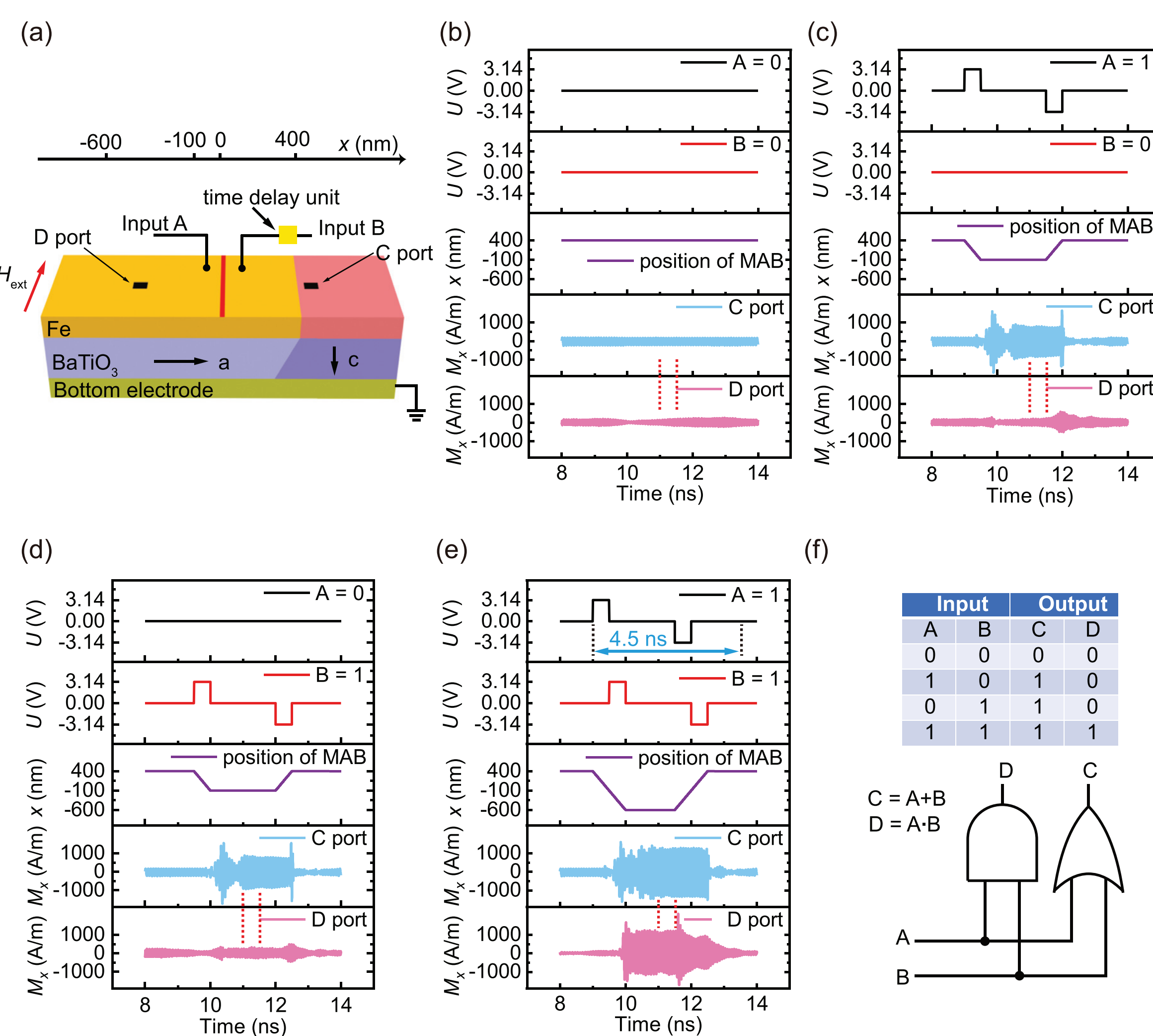

Input		Output	
A	B	C	D
0	0	0	0
1	0	1	0
0	1	1	0
1	1	1	1

FIG. 3. (a) Schematic diagram of the AND–OR gate. Initially, the MAB is set at $x = 400$ nm. Inputs A and B are the input ports, and input B includes a time delay unit that can delay the input signal for 0.5 ns. C and D ports are output ports. The bottom electrode is grounding. The simulation results of the AND–OR gate with different inputs are shown in (b)–(e), respectively. The amplitudes of SWs in 11–11.5 ns are the logic operation results, and the time domain is marked by the red dashed lines. Finishing one logic operation needs 4.5 ns. (f) The truth table of the AND–OR gate.

is also shown in Fig. 3(c). In 9–9.5 ns, the MAB is driven from $x = 400$ nm to $x = -100$ nm. After oscillation in 9.5–11 ns, the amplitudes of SWs at C and D represent C = 1 and D = 0 in the time range of 11–11.5 ns, marked by the red dashed lines. After that, the negative pulse drives the MAB back to $x = 400$ nm during 11.5–12 ns. The outputs will be the same as the initial, and one whole logical operation is finished. Figure 3(d) shows the simulation result of A = 0 and B = 1. It is very similar to the previous operation. The only difference is the 0.5 ns delay of the voltage pulse in the B port. However, the outputs of ports C and D are still 1 and 0, respectively. If A and B ports are both 1, the driving time of the MAB will be 1 ns due to the 0.5 ns delay between A and B shown in Fig. 3(e). The MAB is driven to $x = -600$ nm from $x = 400$ nm during the period of 9–10 ns. The amplitudes of SWs for ports C and D are over 1000 A/m at the time range of 11–11.5 ns. The operation results of C and D are both 1. Then, the MAB is driven back to $x = 400$ nm during 11.5–12.5 ns. It should be mentioned that the amplitude of the SWs in the C port at 11–11.5 ns is a bit larger than that in Figs. 3(c) and 3(d), which mainly arises from the weaker interference between the reflected SWs from the MAB and the initial SWs. In short summary, the logic operation of the AND–OR gate can be divided into three stages: preparation before output (9–11 ns), output (11–11.5 ns), and reset (11.5–13.5 ns). The truth table of the AND–OR gate is shown in Fig. 3(f). The input A and B and output C compose an OR gate while the input A and B and output D compose an AND gate.

In order to implement full Boolean logic operation, we also need the NAND and NOR gates. Figure 4(a) is the schematic of the dual function NAND–NOR gate. Here, the initial MAB is set at $x = -600$ nm. The main change of the NAND–NOR gate is that the two input ports A and B are connected with the bottom electrode, and the Fe layer is grounding. The output ports and source port are the same with the AND–OR

© Author(s) 2022

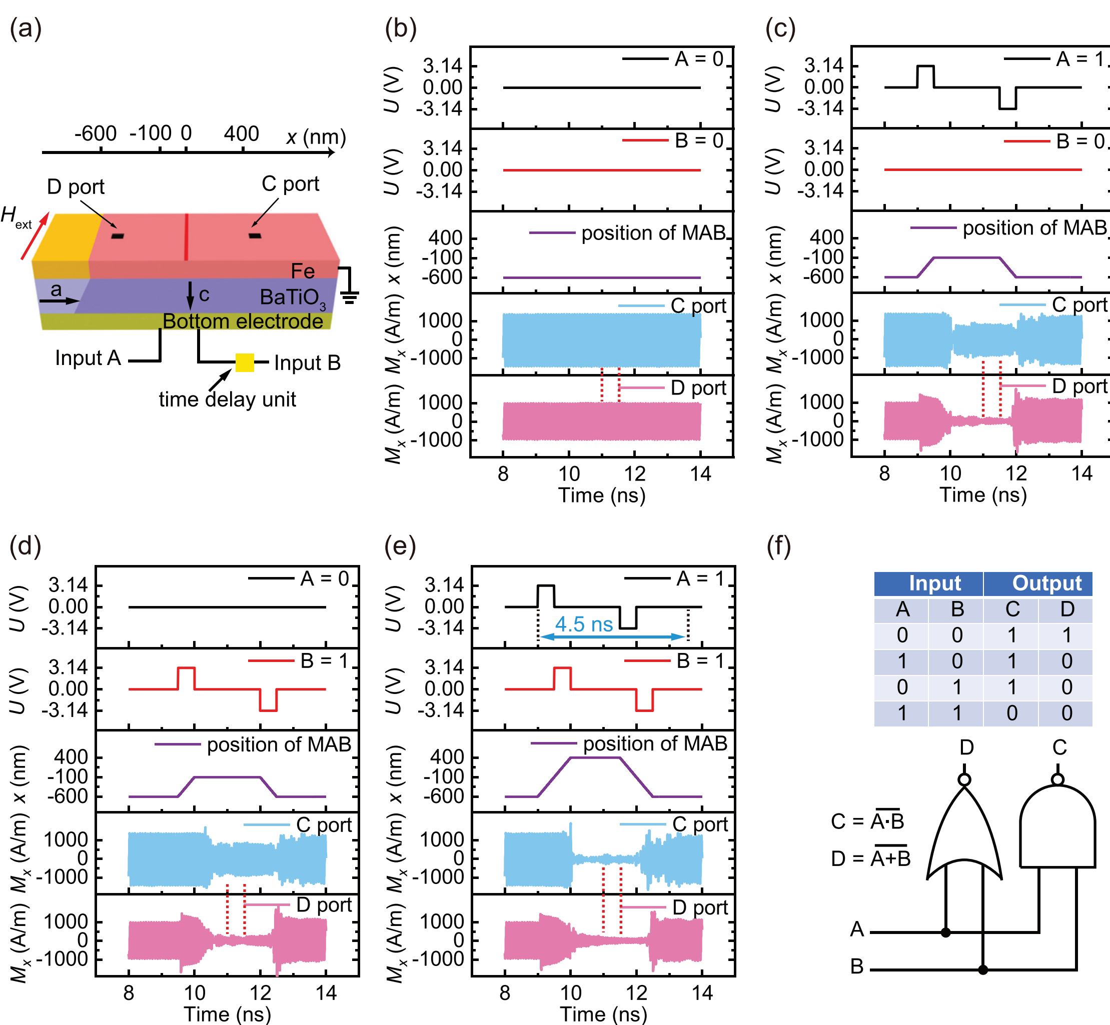

FIG. 4. (a) Schematic diagram of the NAND–NOR gate. Initially, the MAB is set at $x = -600$ nm. The Fe film is grounding, and the input voltage signals are injected from the bottom electrode. Other configurations and the input signals are the same as the AND–OR gate. The simulation results of the NAND–NOR gate with different inputs are shown in (b)–(e). The amplitudes of SWs in 11–11.5 ns are the logic operation results, and the time domain is marked by the red dashed lines. Finishing one logic operation needs 4.5 ns. (f) The truth table of the NAND–NOR gate.

gate. When A and B are both 0, the MAB keeps still at $x = -600$ nm. When only one of A and B is 1, the MAB is driven to $x = -100$ nm for logic operation and then driven back to reset. When A and B are both 1, the MAB is driven to $x = 400$ nm for logic operation and then driven back to reset. The simulation results of the NAND–NOR logic gate with different inputs are shown in Figs. 4(b)–4(e). The output result of A = 0 and B = 0 is shown in Fig. 4(b). The MAB is still at $x = -600$ nm because of the zero-field force. The amplitudes of the SWs are over 1000 A/m, both for C and D ports. This indicates that the output ports C and D are both 1. The simulation result of A = 1 and B = 0 is shown in Fig. 4(c). The MAB is driven from $x = -600$ nm to $x = -100$ nm for a positive pulse during 9–9.5 ns. Then, the amplitude of the SWs at the C port is slightly reduced before the negative reset pulse, which can be explained by the interference between the reflected SWs from MAB and the initial SWs. For the D port, the amplitude of the SWs is almost vanishing. So we can recognize the output C = 1 and D = 0 before the reset of the MAB. Figure 4(d) shows the simulation result for A = 0 and B = 1. The output is the same as A = 1 and B = 0. The last configuration of A = 1 and B = 1 is shown in Fig. 4(e). In 9–10 ns, the MAB is driven to $x = 400$ nm from $x = -600$ nm. After oscillation in 10–11 ns, the amplitudes of C and D in 11–11.5 ns are the operation result representing C = 0 and D = 0. In 11.5–12.5 ns, the MAB is driven back to $x = -600$ nm. After oscillation in 12.5–13.5 ns, one logic operation is finished. The logic operation of the NAND–NOR gate can also be divided into three stages, preparation before output (9–11 ns), output (11–11.5 ns), and reset (11.5–13.5 ns). One circle logic operation needs 4.5 ns. The truth table of the NAND–NOR gate is listed in Fig. 4(f). The input A and B and output C compose a NAND gate, while the input A and B and output D compose a NOR gate.

© Author(s) 2022

In conclusion, we propose dual function SW logic gates based on the motion of the MAB controlled by the electric field. AND–OR gate and NAND–NOR gate are validated by micromagnetic simulation. Owing to the inherent dual function, the proposed SW logic gates have potential of building low power consumption and high density devices. Our results will also motivate further experimental studies for the development of dual function SW devices.

See the supplementary material for the formulas of the dispersion relation of SWs propagating in cubic and uniaxial anisotropy regions.

This work was partially supported by the National Key Research Program of China (Grant No. 2017YFA0206200), Natural Science Foundation of China (Grant No. 11974268), the International Postdoctoral Exchange Fellowship Program (No. 20190083), the Natural Science Foundation of Shaanxi Province (No. 2021JM-022), Japan Society for the Promotion of Science (JSPS) KAKENHI (Grant Nos. 17H06227 and 21H05021), and Japan Science and Technology Agency (JST) CREST (No. JPMJCR18J1).

AUTHOR DECLARATIONS

Conflict of Interest

The authors have no conflicts to disclose.

DATA AVAILABILITY

The data that support the findings of this study are available from the corresponding author upon reasonable request.

REFERENCES

[1]E. Vogel, Nat. Nanotechnol. **2**, 25–32 (2007).
[2]T. N. Theis and H. P. Wong, Comput. Sci. Eng. **19**, 41–50 (2017).
[3]A. Khitun and K. L. Wang, Superlattices Microstruct. **38**, 184–200 (2005).
[4]S. Klingler, P. Pirro, T. Brächer, B. Leven, B. Hillebrands, and A. V. Chumak, Appl. Phys. Lett. **105**, 152410 (2014).
[5]S. Klingler, P. Pirro, T. Brächer, B. Leven, B. Hillebrands, and A. V. Chumak, Appl. Phys. Lett. **106**, 212406 (2015).
[6]T. Fischer, M. Kewenig, D. A. Bozhko, A. A. Serga, I. I. Syvorotka, F. Ciubotaru, C. Adelmann, B. Hillebrands, and A. V. Chumak, Appl. Phys. Lett. **110**, 152401 (2017).
[7]M. P. Kostylev, A. A. Serga, T. Schneider, B. Leven, and B. Hillebrands, Appl. Phys. Lett. **87**, 153501 (2005).
[8]T. Schneider, A. A. Serga, B. Leven, B. Hillebrands, R. L. Stamps, and M. P. Kostylev, Appl. Phys. Lett. **92**, 022505 (2008).
[9]K.-S. Lee and S.-K. Kim, J. Appl. Phys. **104**, 053909 (2008).
[10]M. Jamali, J. H. Kwon, S. M. Seo, K. J. Lee, and H. Yang, Sci. Rep. **3**, 3160 (2013).
[11]J. Lan, W. Yu, and J. Xiao, Nat. Commun. **8**, 178 (2017).
[12]W. Yu, J. Lan, and J. Xiao, Phys. Rev. Appl. **13**, 024055 (2020).
[13]Q. Wang, A. V. Chumak, L. Jin, H. Zhang, B. Hillebrands, and Z. Zhong, Phys. Rev. B **95**, 134433 (2017).
[14]B. Rana and Y. Otani, Phys. Rev. Appl. **9**, 014033 (2018).
[15]B. Rana and Y. Otani, Commun. Phys. **2**, 90 (2019).
[16]C.-G. Duan, J. P. Velev, R. F. Sabirianov, Z. Zhu, J. Chu, S. S. Jaswal, and E. Y. Tsymbal, Phys. Rev. Lett. **101**, 137201 (2008).
[17]M. Tsujikawa and T. Oda, Phys. Rev. Lett. **102**, 247203 (2009).
[18]N. A. Spaldin and M. Fiebig, Science **309**, 391–392 (2005).
[19]T. Taniyama, J. Phys.: Condens. Matter **27**, 504001 (2015).
[20]C. Song, B. Cui, F. Li, X. Zhou, and F. Pan, Prog. Mater. Sci. **87**, 33–82 (2017).
[21]M. Balinskiy, A. C. Chavez, A. Barra, H. Chiang, G. P. Carman, and A. Khitun, Sci. Rep. **8**, 10867 (2018).
[22]A. V. Sadovnikov, A. A. Grachev, S. E. Sheshukova, Y. P. Sharaevskii, A. A. Serdobintsev, D. M. Mitin, and S. A. Nikitov, Phys. Rev. Lett. **120**, 257203 (2018).
[23]G. Dong, S. Li, M. Yao, Z. Zhou, Y.-Q. Zhang, X. Han, Z. Luo, J. Yao, B. Peng, Z. Hu, H. Huang, T. Jia, J. Li, W. Ren, Z.-G. Ye, X. Ding, J. Sun, C.-W. Nan, L.-Q. Chen, J. Li, and M. Liu, Science **366**, 475–479 (2019).
[24]C.-G. Duan, S. S. Jaswal, and E. Y. Tsymbal, Phys. Rev. Lett. **97**, 047201 (2006).
[25]G. Venkataiah, Y. Shirahata, M. Itoh, and T. Taniyama, Appl. Phys. Lett. **99**, 102506 (2011).
[26]G. Radaelli, D. Petti, E. Plekhanov, I. Fina, P. Torelli, B. R. Salles, M. Cantoni, C. Rinaldi, D. Gutiérrez, G. Panaccione, M. Varela, S. Picozzi, J. Fontcuberta, and R. Bertacco, Nat. Commun. **5**, 3404 (2014).
[27]H. Qin, R. Dreyer, G. Woltersdorf, T. Taniyama, and S. van Dijken, Adv. Mater. **33**, 2100646 (2021).
[28]A. Vansteenkiste, J. Leliaert, M. Dvornik, M. Helsen, F. Garcia-Sanchez, and B. Van Waeyenberge, AIP Adv. **4**, 107133 (2014).
[29]R. W. Damon and J. R. Eshbach, J. Phys. Chem. Solids **19**, 308–320 (1961).
[30]T. H. E. Lahtinen, Y. Shirahata, L. Yao, K. J. A. Franke, G. Venkataiah, T. Taniyama, and S. van Dijken, Appl. Phys. Lett. **101**, 262405 (2012).
[31]X. Zhang, T. Hashimoto, and D. C. Joy, Appl. Phys. Lett. **60**, 784–786 (1992).
[32]J. Hlinka and P. Márton, Phys. Rev. B **74**, 104104 (2006).
[33]Q. Zhang and W. A. Goddard, Appl. Phys. Lett. **89**, 182903 (2006).
[34]K. J. A. Franke, B. Van de Wiele, Y. Shirahata, S. J. Hämäläinen, T. Taniyama, and S. van Dijken, Phys. Rev. X **5**, 011010 (2015).
[35]D. Kumar, O. Dmytriiev, S. Ponraj, and A. Barman, J. Phys. D **45**, 015001 (2012).
[36]G. Venkat, D. Kumar, M. Franchin, O. Dmytriiev, M. Mruczkiewicz, H. Fangohr, A. Barman, M. Krawczyk, and A. Prabhakar, IEEE Trans. Magn. **49**, 524–529 (2013).
[37]H. L. Stadler and P. J. Zachmanidis, J. Appl. Phys. **34**, 3255–3260 (1963).
[38]V. Boddu, F. Endres, and P. Steinmann, Sci. Rep. **7**, 806 (2017).
[39]A. K. Tagantsev, L. E. Cross, and J. Fousek, *Domains in Ferroic Crystals and Thin Films* (Springer, New York, 2010), p. 369.

© Author(s) 2022